



Performance of individual cells in polymer electrolyte membrane fuel cell stack under-load cycling conditions



A. Bose^{a,*}, P. Babburi^{b,1}, R. Kumar^c, D. Myers^c, J. Mawdsley^c, J. Milhuff^c

^a Department of Engineering Technology and Texas Center for Superconductivity, University of Houston, Houston, TX 77204, USA

^b 1500 Harbour Dr, Unit 1J, Wheeling, IL 60090, USA

^c Chemical Sciences and Engineering Division, Argonne National Laboratory, 9700S Cass Avenue, Argonne, IL 60439, USA

H I G H L I G H T S

- Stack degradation at single cells level was assessed using DOE load cycling protocol.
- An irreversible degradation of stack performance was observed after 480 h.
- Observed kinetic and mass transport losses were largely dominated at the end cells.
- Kinetic losses were primarily caused by the loss of ECSA.
- Durability of ~1700 h can be estimated based on the initial degradation profile.

A R T I C L E I N F O

Article history:

Received 20 April 2013

Accepted 30 May 2013

Available online 10 June 2013

Keywords:

Polymer electrolyte fuel cells

Performance degradation

Dynamic load cycling

Durability

A B S T R A C T

The performance of a ten-cell 50 cm² 100 W polymer electrolyte membrane fuel cell (PEMFC) stack was evaluated under dynamic load cycling conditions utilizing the 2005 United States Department of Energy durability test protocol for PEFCs. An enhancement of performance was observed during the first 240 h, while an irreversible degradation of stack performance was observed after 480 h (~4700 cycles). In particular, the stack voltage at 100 mA cm⁻² was decreased by 2.8% after 480 h and individual cell voltage was decreased up to 8%. An analysis of cell overpotentials for activation, Ohmic, and mass transport losses revealed that the predominant source of performance degradation was due to kinetic losses. The loss of catalyst utilization was estimated to be 39% based on the electrochemically active surface area (ECSA) measurements. Electron microscopic images of some of the cells showed growth in cathode Pt particle size from 5.3 to 6.2 nm. However, these microscopic images did not show any membrane damage or electrode thinning. Severe degradation of both the anode and cathode silicone gasket seals was observed during the durability test.

© 2013 Elsevier B.V. All rights reserved.

1. Introduction

Polymer electrolyte membrane fuel cells (PEMFCs) represent a promising and viable alternative power source for transportation and other applications [1]. PEMFCs offer high power density and greater efficiency at low operating temperatures. A few challenges of this clean energy technology for transportation applications, including the durability of cell stacks, have been highlighted [2,3]. The potential for achieving the automotive application target of 5000 operating hours [4,5] has been extrapolated based on tests of

single cells, but the reported durability of existing stacks is considerably shorter, about 2000 h [6]. Several studies have documented causal factors affecting the observed performance degradation at the single cell level [7–9]. Multi-cell stacks, however, encounter conditions and stresses different from those encountered in single cells, including cell-to-cell variations in reactant flows, water distribution, membrane humidification, temperature, and compression [10,11]. There are relatively a few studies of PEMFC stack degradation documented in the extant literature, and these studies have primarily evaluated stacks operating under constant current or constant voltage conditions [9,12–15]. In transportation and many other applications, fuel cell systems must meet wide variations in power demand. For example, average cell voltages may vary rapidly from 0.6 to 0.9 V in the automotive application.

* Corresponding author. Tel.: +1 713 743 5765; fax: +1 713 743 4032.

E-mail address: abbpose@uh.edu (A. Bose).

¹ Current address.

We have taken a systematic approach to understand possible reasons for loss of performance at various stages of cell operations. In our earlier work, we demonstrated that cell performance depends on the curing process during fabrication even when every component of a given cell's composition is kept invariant [16]. The objective of the present work is to analyze sources of stack degradation under varying load conditions using a 100 W 10-cell stack by applying various diagnostic techniques to assess the relative impacts of changes in the electrochemically active surface area (ECSA) of cathode catalyst, Ohmic resistance, and mass transport resistance of individual cells during the durability test. Since the cell performance is largely controlled by the oxygen reduction kinetics, this study was concentrated on cathodes.

2. Experimental

2.1. Stack descriptions and data acquisition

A 10-cell hydrogen–oxygen polymer electrolyte research fuel cell stack with 48.5 cm² cell active area was obtained from H2Economy (Yerevan, Armenia). The stack contained Nafion115[®] membrane with 0.5 mg Pt cm^{−2} loading each at the anode and cathode (30% Pt on Vulcan XC-72). The flow-field was double serpentine. The stack was rated to deliver 100 W peak power at 6 V at a nominal operating temperature of 65 °C, with the anode and cathode at 0.75 and 0.9 bar gauge, respectively. Heating the stack was achieved through thermodynamic and resistive losses. Cooling the stack was achieved through fan cooling facilitated by channels drilled through the centers of the third and seventh bipolar plates. The cells were numbered consecutively from 1 to 10, with Cell 1 proximal to the stack gas inlets and Cell 10 proximal to the gas outlets.

A fuel cell (FC) test stand (Scribner 850e) was used to measure polarization curves, control the hydrogen and oxygen flow rates, humidity levels, and monitor temperatures. To enable monitoring of the individual cell performances and conditions, voltage and thermocouple leads are incorporated into each bipolar plate and a thermocouple into one of the cooling channels. The temperature of the stack was monitored in the innermost air cooling hole. Altogether these 10 voltage leads and 12 thermocouples are connected to a multi-meter (Agilent Datalogger), and were monitored on a computer using the Agilent Datalogger software. The individual cell voltages were monitored by the digital multi-meter.

2.2. Stack performance verification and dynamic load test protocol

The initial stack performance was verified under operating conditions recommended by the vendor. These conditions include stack temperature of 65 °C, hydrogen input and humidifier temperature of 50 °C, oxygen input and humidifier temperature of 55 °C, constant flow of 1.24 SLPM hydrogen at 0.75 bar gauge, and 1.18 SLPM oxygen at 0.9 bar gauge. These flow rates equate to hydrogen and oxygen stoichiometry of 1.05 and 2.0, respectively, at 100 W, the rated power of the stack. At the start of a test, the stack was heated to the operating temperature of 65 °C by holding it at a constant potential of 7.0 V before applying the desired test protocol, during which the stack temperature usually decreased. The initial stack polarization curve was identical to that provided by the vendor.

The dynamic load cycling protocol established by the U.S. Department of Energy (DOE) was used to assess the long-term performance of PEMFC stacks under conditions reflecting the automotive application [8,17]. Briefly, the test protocol involves cyclically stepping through a series of currents with periodic interruption of the cycling for polarization measurements and diagnostics. According to the protocol, the definition of stack end-of-

Table 1

DOE-recommended generalized current density vs. time for the dynamic load test protocol [8,16].

| Step | Duration (s) | C _{XX} | Step | Duration (s) | C _{XX} |
|------|--------------|-----------------|------|--------------|-----------------|
| 1 | 15 | OCV | 9 | 20 | C ₇₅ |
| 2 | 25 | C ₈₀ | 10 | 15 | C ₈₈ |
| 3 | 20 | C ₇₅ | 11 | 35 | C ₈₀ |
| 4 | 15 | C ₈₈ | 12 | 20 | C ₆₀ |
| 5 | 24 | C ₈₀ | 13 | 35 | C ₆₅ |
| 6 | 20 | C ₇₅ | 14 | 8 | C ₈₈ |
| 7 | 15 | C ₈₈ | 15 | 35 | C ₇₅ |
| 8 | 25 | C ₈₀ | 16 | 40 | C ₈₈ |

Abbreviations used: XX=stack voltage*10 (V), C_{xx} refers to current densities at various cell voltages (for example, C₈₀ is the current density at a cell voltage of 0.8 V), and OCV = open circuit voltage.

life is a decay of ≥10% of the average cell voltage at all current densities. The various steps in the dynamic load test protocol are shown Table 1 [8,17]. The current densities at the various steps are defined by the measured current densities at the specified cell voltages obtained in the initial stack polarization measurement. The initial stack polarization curve was used to establish the current steps for the load test profile at stack voltages of 8.8, 8.0, 7.5, 6.5, and 6.0 V. The current values at these voltages are designated as C₈₈, C₈₀, C₇₅, C₆₅, and C₆₀, respectively, as listed in Table 1. These current densities and time intervals were then used for the load cycling tests. Constant stoichiometric flow ratios of 1.05 for H₂ and 2.0 for O₂ were used during each step. The current density, fuel and oxidant gas inlet flow rates, temperatures, and humidifier temperatures were controlled, and the corresponding individual cell voltages and temperatures were recorded. The dynamic testing was interrupted at 240 h and 480 h to perform diagnostic tests, as discussed below.

2.3. In-situ diagnostics

After 240 h and 480 h of dynamic load cycling, stack polarization curves were measured in the controlled-current mode. The increasing current portions of these curves are shown in Fig. 1. The maximum current density was constrained to ~300 mA cm^{−2} due to gas flow rate limitations inherent in the test equipment. The total resistance of the stack was obtained by using the current interrupt

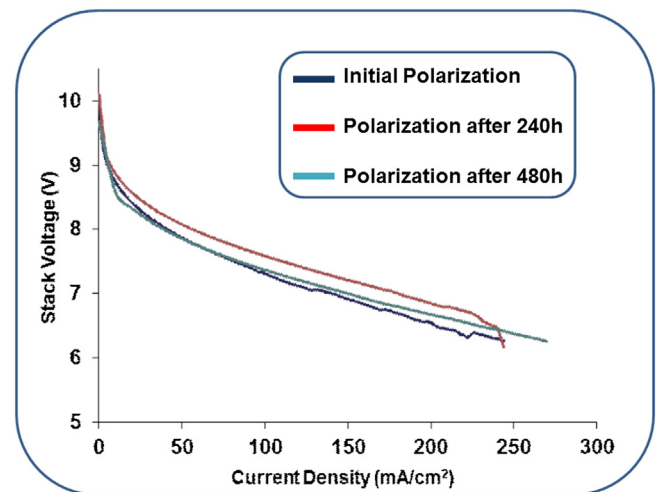


Fig. 1. Polarization curves for the 10-cell stack recorded at 0, 240, and 480 h of dynamic stress testing. Test conditions: pressures, anode/cathode, 0.75/0.9 bar gauge; temperatures, cell = 65 °C, H₂ humidifier = 50 °C, O₂ humidifier = 55 °C; stoichiometry, H₂/O₂ = 1.05/2.0.

technique at all current levels during the acquisition of polarization data. Resistances of the individual cells were determined by EIS by connecting the voltage leads sequentially to the anode and cathode bipolar plates of each cell while drawing a constant current of 100 mA cm^{-2} from the stack.

The electrochemically active surface area (ECSA) of the cathode platinum electro-catalyst and the hydrogen crossover rate through the membrane were determined using cyclic voltammetry using a Solartron 1287 potentiostat room temperature with humidified hydrogen on the anode side and humidified nitrogen on the cathode side (relative humidity = 100%). The potentials on the cells were scanned between 0.0 V and 0.8 V at 2 mV s^{-1} until a reproducible voltammogram was obtained. The ECSA was determined from the hydrogen desorption region of the voltammogram, assuming adsorption charge of $210 \text{ } \mu\text{C cm}^{-2}$ of the ECSA [18]. The hydrogen crossover was determined using the steady-state anodic current in 0.4–0.5 V region, corrected for the double layer charging current [19].

During the cycling tests, the cathode exit gas was cooled in a water-chilled condenser and the condensate was collected periodically. The condensate was analyzed for Pt content using inductively coupled plasma mass spectrometry (ICP-MS, FisonsQuadrupole PQII⁺ ICPMS, and VG elemental high-resolution AXIOM ICPMS), which has a Pt detection limit of 1 ppt.

2.4. Diagnosis of stack voltage losses

The relationship between fuel cell voltage and current density is described by the following equation [20]:

$$V(i) = E_{\text{rev}} - (\eta_{\text{act},\text{O}_2} + \eta_{\text{act},\text{H}_2} + \eta_{\text{conc},\text{O}_2} + \eta_{\text{conc},\text{H}_2} + iR) \quad (1)$$

E_{rev} is the thermodynamic potential for the O_2/H_2 reaction, defined by the free energy change of the fuel cell reaction and the reactant concentrations, and i is the cell's current density. The entities represented by η_{act} are the activation overpotentials or losses due to the kinetics of oxygen reduction and hydrogen oxidation reactions. Likewise, η_{conc} values are the overpotentials due to changes in reactant concentrations at the catalytic sites from their bulk gas concentrations (mass transfer losses). The iR term is the total resistive loss due to proton transport in the membrane, electron transport in the electrode layer, the gas diffusion layer, the bipolar plate, and the resistances at the interfaces between these components [21].

The kinetics of the cathodic reaction are approximately seven orders of magnitude lower than those of the anodic reaction, and therefore dominate the cell kinetic losses when adequate anode catalyst loadings are used and the fuel gas is pure hydrogen. The activation overpotential for the cathode kinetics is described by [20]:

$$\eta_{\text{act},\text{O}_2} = (2.303RT/\alpha_c F) \log i_0 - (2.303RT/\alpha_c F) \log i^* L_{\text{ca}}^* A_{\text{Pt,el}} \quad (2)$$

$2.303 RT/\alpha_c F$ is the Tafel slope measuring approximately 67 mV dec^{-1} at 65°C [22], and i_0 is the exchange current density for the oxygen reduction reaction (ORR), which is approximately $0.8\text{--}9 \times 10^{-9} \text{ A cm}^{-2}$ Pt active area (at $60\text{--}95^\circ\text{C}$ and 101.3 kPa O_2 pressure) [18,23], i is the cell geometric current density, L_{ca} is the cathode Pt loading (mg Pt cm^{-2}), and $A_{\text{Pt,el}}$ is the cathode Pt electrochemically active surface area ($\text{cm}^2 \text{ Pt (mg Pt)}^{-1}$). Due to the low exchange current density for the oxygen reduction reaction (ORR), oxide formation on the platinum surface, and hydrogen crossover through the perfluorosulfonic acid membrane, the open circuit voltage is significantly lower than E_{rev} [18]. Under conditions of

adequate reactant supply, transport to the catalyst sites, and adequate humidification of the perfluorosulfonic acid ionomer and membrane, the cathode activation overpotential dominates cell losses at low current densities [18].

A useful method for determining the sources of cell and stack voltage losses is to correct the measured cell and stack voltages for iR losses, with the value of R determined independently using current interrupt and/or high frequency impedance measurements, and to plot this iR -corrected voltage versus current density [18,24]. At low current densities, the oxidation current on the cathode resulting from hydrogen crossing through the membrane can be significant in comparison to the ORR current. To isolate the contribution of ORR kinetics to cell voltage losses, measured cell currents must be corrected for the so-called “hydrogen crossover current” by adding this current to the measured value [18,24]. A plot of the iR -corrected cell voltages vs. the logarithm of the hydrogen crossover-corrected current density should be linear, with a slope corresponding to the Tafel slope of 67 mV dec^{-1} if the voltage losses are controlled solely (or primarily) by the kinetics of the oxygen reduction reaction [18,24]. As shown in equation (1), deviation from this slope indicates that concentration polarization or mass transfer resistances ($\eta_{\text{conc},\text{O}_2}$ or $\eta_{\text{conc},\text{H}_2}$) are contributing significantly to cell voltage losses.

In this analysis, “kinetic loss” is defined as the difference between the theoretically reversible potential (1.199 V at 65°C) and the voltage at 100 mA cm^{-2} , obtained from an extrapolation of a linear fit of the iR and hydrogen crossover-corrected voltage versus the logarithm of the current density plot in the low current density region. The difference between this extrapolated voltage and the measured iR -corrected voltage is attributable to mass transfer losses.

2.5. Post-test diagnostics

At 480 h into the test under load cycling conditions, Cell 5 failed and lost voltage completely, and all cells downstream of Cell 5 (Cells 6–10) showed widely fluctuating voltages. At this time, the test was terminated and the stack disassembled. The membrane-electrode assemblies (MEAs) and gaskets were examined visually and with an optical microscope. In addition, three cells (1, 5, and 7), including one upstream and one downstream of the failed cell, were examined using scanning electron microscopy (SEM) and energy dispersive X-ray (EDX) spectroscopy for elemental mapping. For this examination, approximately 1-cm^2 pieces were cut out of the center of each cell and encased in epoxy (Epothin[®], Buehler), revealing a cross-section of each MEA. These epoxy-mounted samples were then polished flat using a vibratory polisher with kerosene as the carrier for the alumina polishing powder.

Separately, the cathode and anode catalyst layers were removed from the MEA of Cell 4 by swelling the MEA in isopropyl alcohol. These electrode materials were then analyzed by powder X-ray diffraction (XRD) to determine the mean crystallite size of the Pt nano-particles using Debye–Scherrer analysis of the widths of the Pt (111) diffraction peaks.

3. Results and discussion

3.1. Stack performance

The steady-state stack polarization curves after 0, 240, and 480 h of load cycling are shown in Fig. 1. These results show an overall performance improvement of 275 mV at 100 mA cm^{-2} and 308 mV at 200 mA cm^{-2} after 240 h. After 480 h of cycling, however, a performance degradation of 218 mV at 100 mA cm^{-2} and 173 mV at 200 mA cm^{-2} was observed. A voltage loss of 2.8% from the maximum performance was observed, which is less than the

10% DOE end-of-life criterion. Based on a linear extrapolation of this degradation rate, the projected 10% end-of-life loss would have been reached at approximately 1700 h. The initial high frequency resistance of the stack, as measured by electrochemical impedance spectroscopy, was $3642 \text{ m}\Omega \text{ cm}^2$, which dropped to $3248 \text{ m}\Omega \text{ cm}^2$ after 240 h of cycling, and then to $2954 \text{ m}\Omega \text{ cm}^2$ after 480 h of cycling. A possible source of decreased high frequency resistance is the improved humidification of the membrane, resulting in decreased resistance to proton transport [18]. A comparison of the iR -corrected stack polarization curves (not shown) indicated that changes in the stack iR losses were neither a major contributor to the stack performance improvement after 240 h nor a major contributor to the observed stack performance losses after 480 h of cycling. The sources of overall stack performance changes with cycling were further explored through individual cell diagnostics at 0, 240, and 480 h of cycling.

The voltage responses of the stack to the load cycling were monitored over time. These data show a gradual decrease in stack voltage at low current density starting at 272 h. For example, the highest voltage measured at 272 h was 9.8 V which decayed to 9.4 V at 300 h. This decay in stack voltage is representative of the decay observed during the rest of the cycling period and correlates with the observed loss in stack OCV.

3.2. Initial individual cell diagnostics

Polarization curves of individual cells are shown in Fig. 2. In constructing these polarization curves, the current density was measured from the stack and voltages for individual cells were separately monitored as described in Section 2.1. Since cells in the stack are connected in a series, the same current is flowing through all the cells which appeared in the abscissa in Fig. 2. The initial polarization curves (Fig. 2a) show that six cells (2–7) were within 100 mV of each other over the entire current density range. The other four cells (1 and 8–10) showed lower performance, up to 230 mV lower than the average cell voltage at 100 mA cm^{-2} . The highest initial voltage losses were observed for the end cells, Cells 1 and 10.

The temperatures of the individual cells varied as much as 10°C during load cycling. Such non-isothermal behavior can occur in a stack due to an uneven dissipation of the total heat produced in the stack also observed in other studies [25,26]. As expected, the end cells, Cell 1 and 10, ran cooler than cells in the middle of the stack due to heat losses through the end plates. The temperatures of the other cells were likely non-uniform due to unequal distribution of the cooling air.

Table 2 lists the measured individual cell high frequency resistances (HFRs) and cathode catalyst ECSAs at 0, 240, and 480 h.

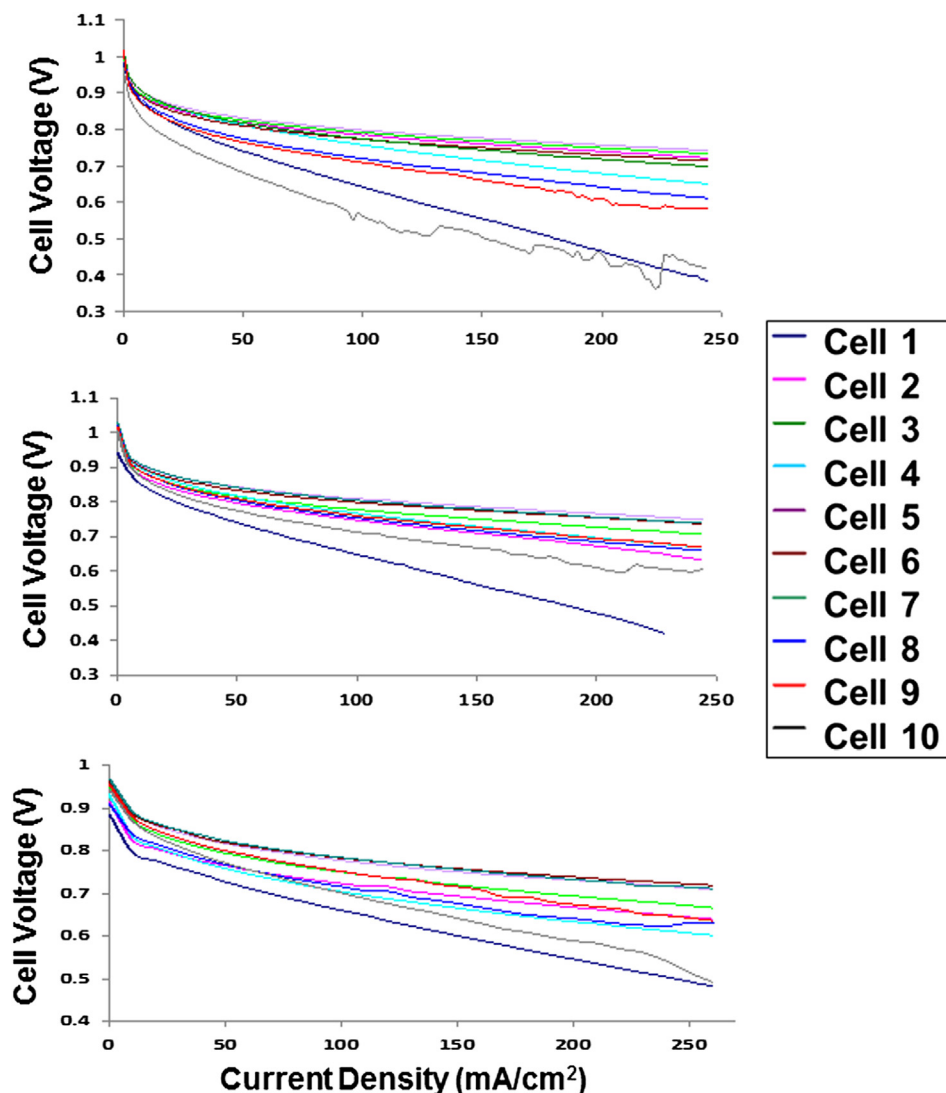


Fig. 2. Individual cell polarization curves (a) initial, (b) after 240 h, (c) after 480 h, under test conditions as in Fig. 1.

Table 2

Individual cell high frequency resistances and ECSA before and after dynamic cycling for 240 and 480 h.

| Cell | High frequency resistance ($\text{m}\Omega \text{ cm}^2$) | | | Electrochemically-active surface area ($\text{m}^2 \text{ g}^{-1}$) | | | % Loss at 480 h |
|-------|---|----------|----------|---|----------|----------|-----------------|
| | Initial | At 240 h | At 480 h | Initial | At 240 h | At 480 h | |
| 1 | 392 | 409 | 381 | 17.1 | ND | ND | ND |
| 2 | 228 | 215 | 235 | 21.8 | 23.3 | 13.9 | 36 |
| 3 | 207 | 213 | 219 | 25 | 30.9 | 13.8 | 45 |
| 4 | 643 | 507 | 452 | 21.5 | 14.7 | 9.4 | 56 |
| 5 | 213 | 218 | 219 | 19.2 | 17.7 | 12.6 | 34 |
| 6 | 197 | 190 | 197 | 20.8 | 23.2 | 15.7 | 25 |
| 7 | 379 | 275 | 265 | 21.3 | ND | 16.4 | 23 |
| 8 | 538 | 415 | 318 | 25 | 8.6 | 5.3 | 79 |
| 9 | 395 | 362 | 304 | 13.1 | 10.5 | 15.3 | N/A |
| 10 | 450 | 442 | 364 | 23.3 | 9.9 | 14.7 | 37 |
| Stack | 3642 | 3248 | 2954 | | | | Avg = 42 |

Abbreviations used: ND, not determined; N/A, not applicable

The initial HFRs show large cell-to-cell variations with only four cells exhibiting HFRs within the normally expected range of $\sim 200 \text{ m}\Omega \text{ cm}^2$ quoted by the stack vendor. A typical specific Ohmic resistance was between 100 and $200 \text{ m}\Omega \text{ cm}^2$ [27]. Notably, Cells 4 and 8 had anomalously high HFRs, possibly due to inadequate humidification of these cells, or excessively high contact resistances between the electrode layers and the membrane. The measured cathode ECSAs showed an average initial value of $20.8 \pm 3.6 \text{ m}^2 \text{ g}^{-1}$, with Cell 9 showing a significantly lower ECSA. This could result from inadequate formation of a triple-phase zone for charge transfer in electrochemical reaction, a defect sometimes introduced during electrode fabrication. The maximum initial ECSA, assuming spherical 5.3 nm particles, was approximately $50 \text{ m}^2 \text{ g}^{-1}$ [28].

The slopes of the iR -corrected voltage vs. log of the hydrogen crossover-corrected current density curves are compared to the theoretically expected slope near the top of Fig. 3. Cells 1 and 10 deviate from the theoretically expected slope of 67 mV dec^{-1} [22] at current densities from 10 to 150 mA cm^{-2} . This suggests that factors other than activation losses, such as mass transfer in the electrodes, are influencing these two cells at the low current densities compared to the other eight cells. As shown in Fig. 4, Cells 1 and 10 also had the lowest initial OCVs. In general, the low cell voltages could be due to uneven gas diffusion, low cell temperature, or water

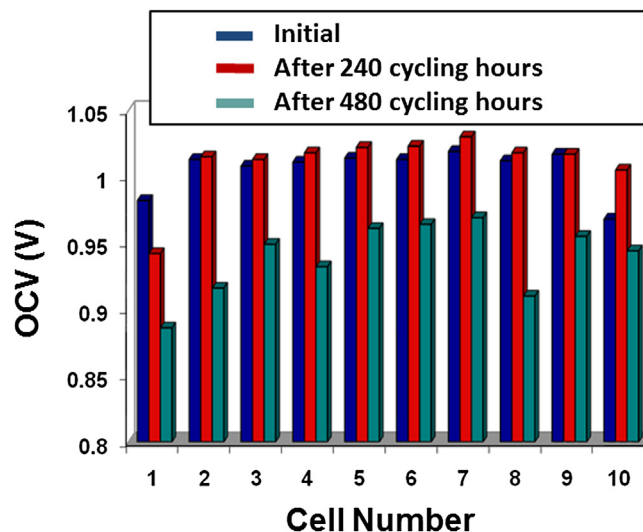


Fig. 4. Comparison of individual cell open circuit voltages (OCVs) during the aging tests showing the large decrease in cell OCVs between 240 and 480 h.

flooding. Our data suggest that the low OCV of these end cells is most likely due to their lower temperatures. Low-end cell temperatures could have led to flooding in the electrode layers, which prevented reactants from reaching the triple-phase-reaction sites. Further, linear sweep voltammogram, LSV data suggest that the lower OCV of Cells 1 and 10 may not be affected by hydrogen crossover because the measured hydrogen crossover rates were nearly identical for all cells, $0.26 \pm 0.04 \text{ mA cm}^{-2}$, and they showed no systematic change as a result of load cycling. Therefore, the lower OCV values in Fig. 4 are most likely associated with the relatively low cell temperatures of the end cells as mentioned earlier. As discussed by Kundu et al. [29], decreases in cathode ECSA impact OCVs due to an increase in the hydrogen crossover rate per active Pt site and the corresponding logarithmic dependence of voltage loss on this rate. However, a comparison of the initial cell OCVs (Fig. 4) and the initial ECSAs (Table 2) shows no correlation between ECSA and OCV. Conversely, a correlation was observed between OCV (Fig. 4) and mass transfer losses. The lower OCVs of the end cells may be due to

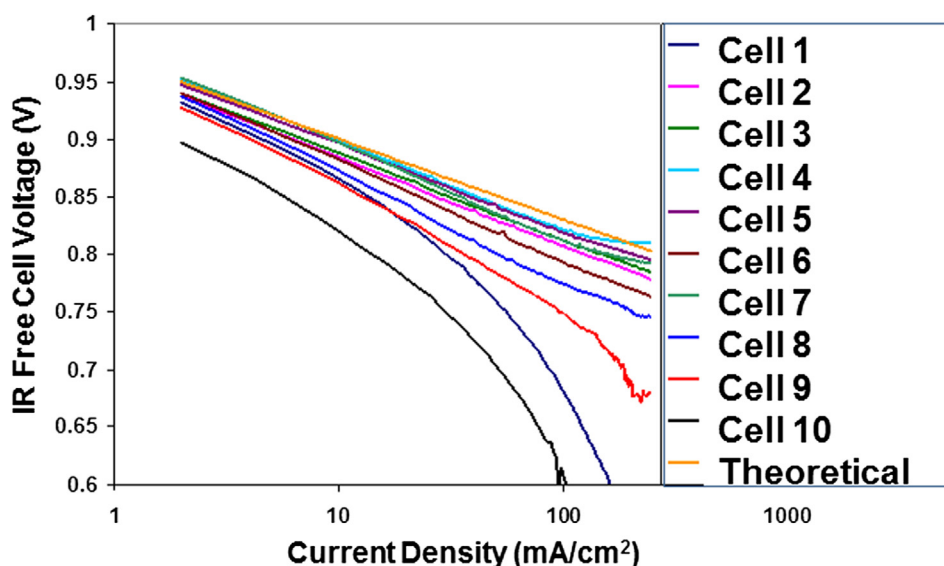


Fig. 3. Initial V versus log i plots of individual cells used to calculate the losses as displayed in Table 2.

significant blockage of catalyst sites due to water accumulation, perhaps caused by the lower temperatures of these cells.

The overall stack voltage decrease was evaluated as 4.644 V at 100 mA cm⁻² based on the theoretical reversible voltage under the experimental conditions. A breakdown of the individual cell kinetic, *iR*, and mass transport contributions to the overall voltage loss is shown in Fig. 5a. These data confirm that cathode kinetic losses dominated voltage losses in all cells. As expected, mass transport losses at 100 mA cm⁻² were minimal in most of the cells, but they were significant in Cells 1 and 10, and to a smaller extent in Cell 9. Resistive losses ranged from 20 to 65 mV at 100 mA cm⁻², with Cells 4 and 8 showing the highest *iR* losses (which improved over time). Based on these data and the known lower temperatures of the end cells, the relatively poor initial performance of Cells 1 and 10 could be due to water accumulation in these cells blocking mass transfer in the gas diffusion layers or the electrodes.

3.3. Diagnosis after 240 cycling hours

Following the initial diagnostic study, the stack was subjected to 240 h of dynamic load cycling. After 240 h, stack polarization, ECSA, and high frequency resistances of the cells were measured using the same conditions applied for the initial diagnostic measurements. As discussed above, the performance of the stack improved after the first 240 h, indicating that the stack had not yet reached its maximum performance at the time of initial characterization, even after the stack conditioning treatment (Fig. 1).

Fig. 5b summarizes the changes in the individual cell voltage losses at 100 mA cm⁻² after 240 h of dynamic load cycling relative to the initial cell performances. The stack voltage showed an

increase of 273 mV at 100 mA cm⁻². More than half of the improvement in performance (55%) is attributable to a decrease in the kinetic and mass transport losses in Cell 10. Cells 5–9 also showed appreciable performance improvement after 240 h, primarily due to a decrease in kinetic losses, which occurred despite decreases in the measured cathode catalyst ECSA for Cells 5, 8, 9, and 10 (Table 2). During this testing period, the average cell high frequency resistance decreased from 364 mΩ cm² to 325 mΩ cm², accounting for ~15% of the total improvement at 100 mA cm⁻², with the bulk of the decrease attributable to Cells 4, 7, and 8.

3.4. Diagnosis after 480 h

Significant performance degradation was observed at the end of 480 h of dynamic load cycling, both in the stack and in all of the cells in the stack (Figs. 1 and 2c). As shown in Fig. 4, a large loss in OCV was observed for all cells, with a total stack OCV loss of 715 mV. This decrease in OCV cannot be attributed to hydrogen crossover because the change in hydrogen crossover was negligible (0.06 mA cm⁻², maximum) throughout the testing period. A relatively low OCV is attributed to the lower temperatures in the end cells. The asymmetric changes of entropy due to the irreversibility of electrochemical reaction and the over-potential on anode and cathode cause a non-uniform heat distribution in the stack resulting in a cell to cell temperature gradient [30]. The loss in OCV, therefore, is most likely caused by the decrease in cathode ECSA by an average of 42%, as shown in Table 2, or by a change in the effective hydrogen or oxygen concentration with cycling. The causes of the severe degradation of the silicon gasket are unknown, internal mixing of the reactants remained a possibility.

Fig. 5c summarizes the changes in the individual cell voltage losses at 100 mA cm⁻² after 480 h of dynamic load cycling, relative to the losses observed after 240 h of cycling. From 240 to 480 h, the kinetic losses at 100 mA cm⁻² increased by 209 mV, and mass transfer losses increased from 106 mV to 152 mV. Notably, a significant increase in mass transfer loss was observed at the outlet end cells (Fig 5c). This significant increase might be related to non-isothermal stack conditions or due to flooding. A small decrease in *iR* losses was observed in six cells, resulting in a total *iR* loss decrease of 30 mV for the stack. Post-test diagnostic results described in Section 3.5 below agree with these data, showing minimal changes in the membrane as a result of 480 h of cycling. The end cells showed the smallest increase in kinetic losses, while all other cells, with the exception of Cell 4, showed comparable degradation of the cathode kinetics.

The increased kinetic losses and decreased OCVs can be attributed, at least in part, to losses in the ECSA of the cathode catalysts. Compared to the initial ECSA values, the individual cell cathode ECSA losses ranged from 23% to 79% (Table 2). Cell 4 showed a greater than average ECSA loss and exhibited a large degradation in the cathode kinetics. The ECSA loss of Cell 8 was the highest at 79%, but it did not result in a higher than average degradation of cathode kinetics. As summarized recently by Shao-Horn et al. [31], ECSA losses may result from several processes, including agglomeration of the electro-catalyst and dissolution of Pt into the cathode effluent. Analyses of the cathode effluent by ICP-MS for Pt content after every 50 h of stack operation showed that Pt was continuously lost into the cathode exhaust during the dynamic load cycling, with a maximum Pt concentration of 34.2 ppb measured in the condensate from the cathode exhaust gases.

3.5. Post-test diagnostic results

Shortly after the stack failed, Cell 5 exhibited 0 V. Post-test visual and optical microscopic examination of the MEAs showed that

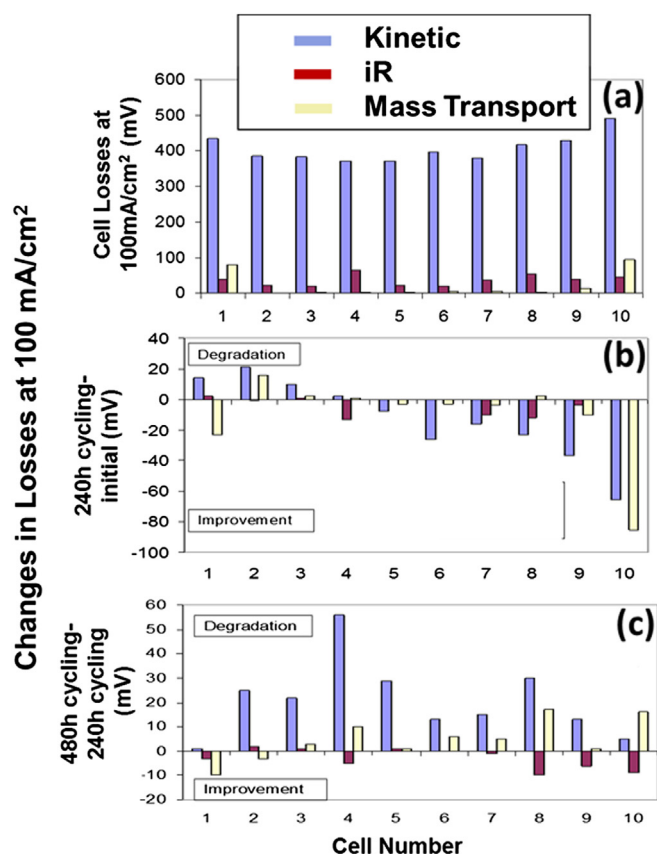


Fig. 5. Major cell losses calculated at 100 mA cm⁻² for each of the 10 cells (a) initial, (b) change between initial and 240 h, and (c) change between 240 and 480 h.

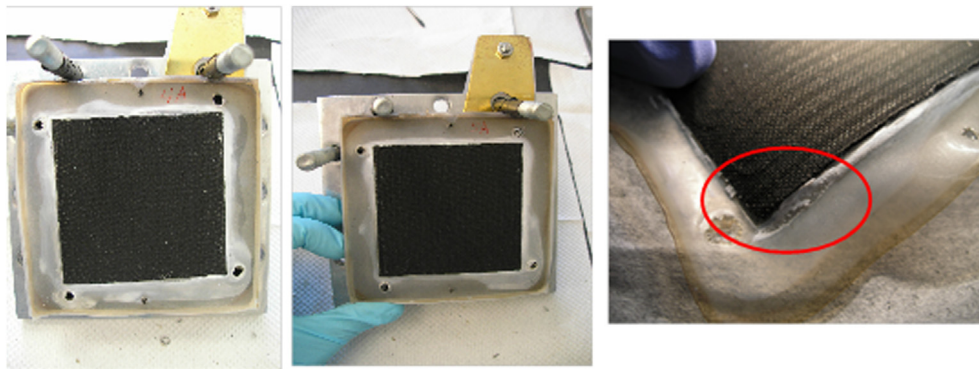


Fig. 6. Post-test photographs of MEAs from Cell 4 (left) and Cell 5 (middle and right) showing degradation of silicone gaskets around the edges.

significant degradation of the anode and cathode silicone gaskets had occurred in all of the cells. Representative photographs of the anode sides of Cells 4 and 5 are shown in Fig. 6. The gasket degradation was particularly severe near the gas outlets, potentially resulting in the direct reaction of hydrogen and oxygen, causing the stack to fail.

The MEAs from Cells 1, 5, and 7 were examined by scanning electron microscopy (SEM) with elemental mapping by EDX to determine if there were differences among them and changes in the thickness of the cell layers, the extent to which the ionomer and Pt/C mixed, and distribution of Pt in the electrode layers. These cells were selected for analysis as Cell 1 was located at the stack inlet, Cell 5

was the one that failed, and Cell 7 was a typical cell. Representative SEM micrographs are shown in Figs. 6–8. The analyses revealed no major differences among the three cells. The perfluorosulfonic acid membrane was $\sim 150\text{-}\mu\text{m}$ thick, but the anode and cathode layers were not uniformly thick across a given cell. The thickness of the electrode layers ranged from 10 to $45\text{ }\mu\text{m}$, and the electrode layers were thinner where they made contact with the gas diffusion layers. Individual particles of platinum could not be resolved, but Pt clusters were observed in the cathode of Cell 1. The ionomer in the electrode layers was well-mixed with the Pt/C, and the Pt/C was uniformly dispersed through the thickness of the electrodes. No thinning of the cathodes compared to the anodes was observed,

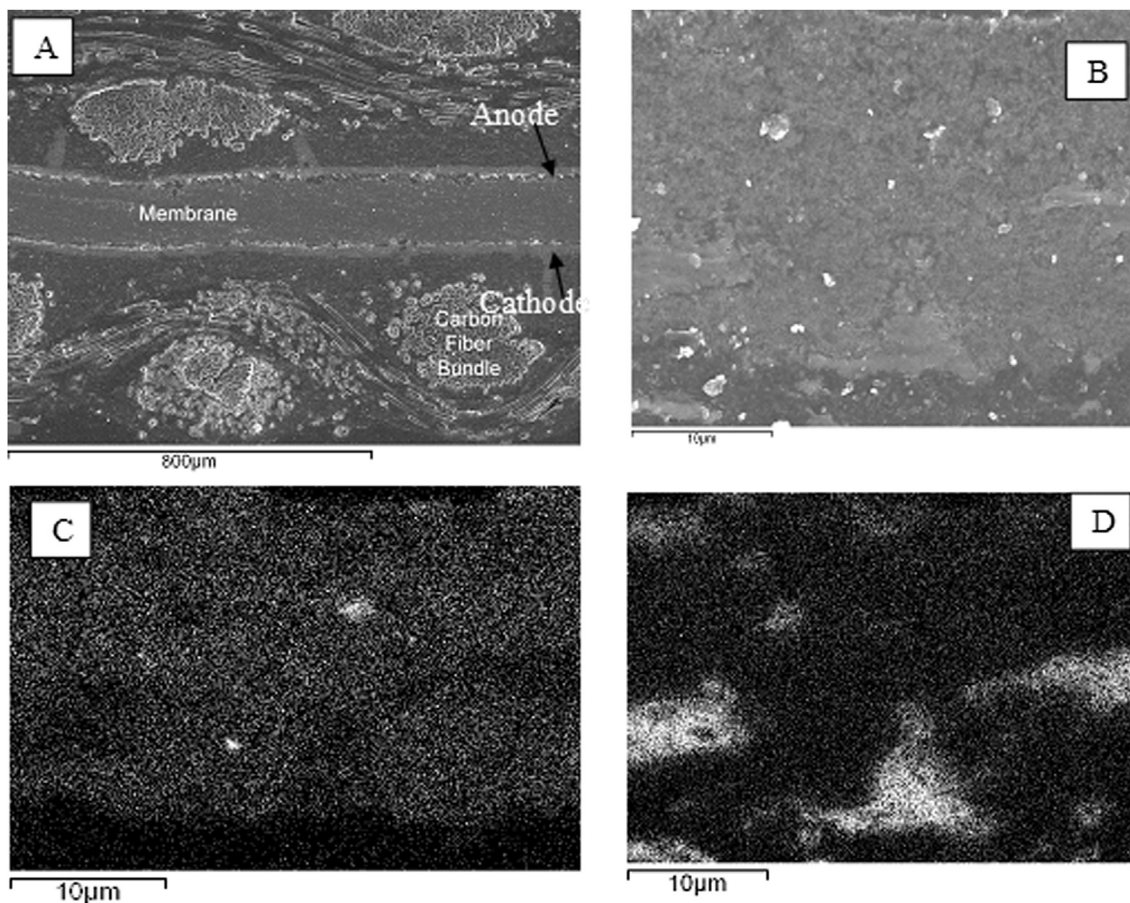


Fig. 7. Images of Cell 1: (A) SEM image of a cross-section; (B) SEM image of a section of the cathode layer (a small swath of the GDL is at the bottom of the image); (C) EDX map of fluorine in the cathode layer of the SEM image in (B) showing where the Nafion is located; and (D) EDX map of Pt in the cathode layer in (B).

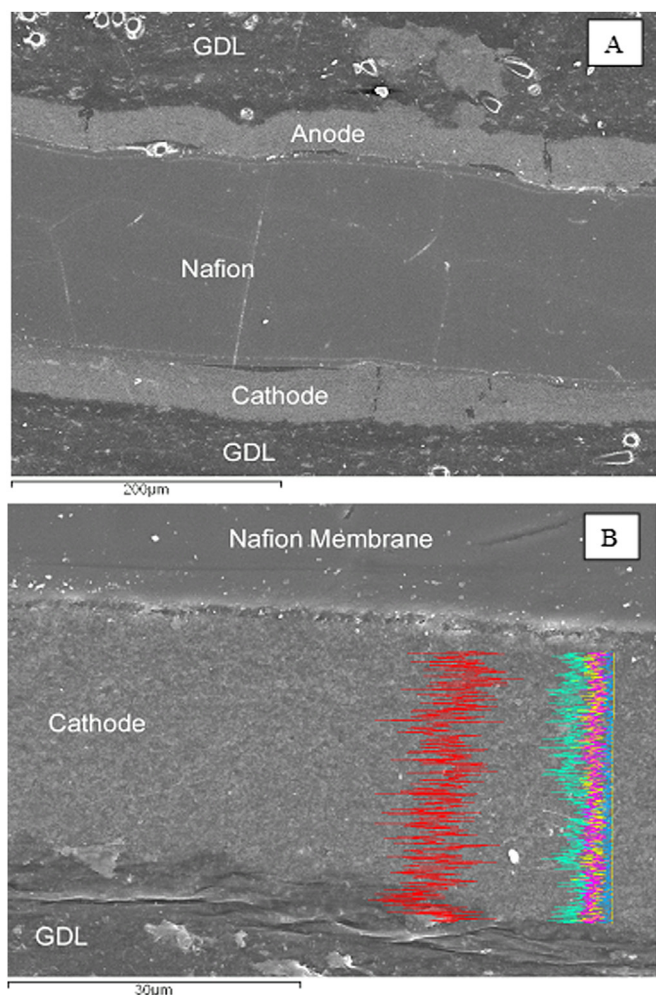


Fig. 8. SEM images of (A) a cross-section of Cell 5, and (B) the cathode of Cell 7 with a superimposed EDX line scan where red = carbon, green = fluorine, pink = platinum (For interpretation of the references to color in this figure legend, the reader is referred to the web version of this article.).

which argues against significant cell degradation due to carbon support oxidation at the high potential of the cathodes. The bonding between the electrodes and the membranes was weak, however, and separation between these layers was often seen.

Post-mortem X-ray diffraction analysis of the cathode and anode catalyst layers of Cell 4 showed that the Pt crystallites have an average diameter of 6.2 nm in the cathode and 5.3 nm in the anode. Assuming negligible change in the size of Pt particles on the anode side [32], the pre-test particle size on cathode is approximated to be 5.3 nm. Thus, the average platinum particle size on cathode had increased from 5.3 nm to 6.2 nm over 480 h of cyclic testing, resulting in a corresponding loss of ECSA. With 5.3 nm size particles initially, the estimated highest possible ECSA on the cathode (assuming spherical Pt particles and utilization of the entire surface area of the sphere) is $\sim 50 \text{ m}^2 \text{ g}^{-1}$, whereas the measured initial average ECSA was only $\sim 21 \text{ m}^2 \text{ g}^{-1}$. Based on this estimate, the initial average cathode catalyst utilization was $\sim 42\%$. With 6.2-nm Pt particles on the cathode after 480 h of testing, the estimated highest possible ECSA is $45 \text{ m}^2 \text{ g}^{-1}$ (assuming negligible Pt mass loss from the cell), whereas the measured ECSA after 480 h of cycling was only $9.4 \text{ m}^2 \text{ g}^{-1}$. Therefore, utilization of the available platinum surface area had dropped from approximately 42% to 21% over the 480 h. In addition to loss of Pt from the cathode, as evidenced by ICP-MS analysis of the condensate from the

cathode effluent, a portion of the decrease in Pt utilization is believed to have occurred by the loss of contact between the Pt particles and the carbon support or the ionomer in the electrode layer [31,33].

4. Conclusions

The effects of dynamic load cycling on individual cells and the importance of prolonged durability test are demonstrated for a commercial 100 W PEMFC. The initial cell overpotentials at 100 mA cm^{-2} were dominated by cathode kinetic losses. Both end cells exhibited some mass transport loss as well. During the first 240 h operation, an improvement in performance of several cells and hence the improvement of stack performance was observed. This enhancement in performance was in keeping with the significant reduction of kinetic losses for all cells, especially for the end cells. Likewise, significant improvements in mass transport loss were also observed for end cells. However, after 480 h cycling, both kinetic and mass transport losses were significantly increased. Although random variation of kinetic loss among cells was observed, significantly larger mass transport loss was confined at the outlet cells perhaps partly related to non-isothermal stack conditions or due to flooding. The increase in kinetic losses for the long-term operation was primarily caused by the loss of electrochemically-active surface area of the Pt electro-catalyst resulting from Pt particle growth and loss of Pt into the cathode effluent. Although the stack end-of-life was indeterminate due to the mechanical failure of silicone gaskets, extrapolation of the initial degradation profile yields an estimate of $\sim 1700 \text{ h}$.

Acknowledgments

Support of this work by the U.S. Department of Transportation (IL 26-7006) and by the U.S. Department of Energy, and Texas Center for Superconductivity at the University of Houston (10EE0003666) is gratefully acknowledged. We would also like to thank Yifen Tsai of Argonne's Analytical Chemistry Laboratory for Pt analyses in the stack effluent. We are grateful to a reviewer who has suggested that flooding might impact end cells due to low temperatures at the anode side.

References

- [1] F. Villatico, F. Zuccari, *Int. J. Hydrogen Energy* 33 (2008) 3235–3242.
- [2] M.F. Mathias, R. Makharia, H.A. Gasteiger, J.J. Conley, T.J. Fuller, C.J. Gittleman, S.S. Kocha, D.P. Miller, C.K. Mittelsteadt, T. Xie, S.G. Yan, P.T. Yu, *Electrochem. Soc. Interface* 14 (2005) 24–35.
- [3] M. Mathias, H.A. Gasteiger, R. Makharia, S.S. Kocha, T.J. Fuller, T. Xie, J. Pisco, *Prepr. ACS Division of Fuel Chemistry, Preprints* 49 (2004) 471–474.
- [4] "Fuel Cells," Fuel Cell Technologies Office Multi-year Research, Development and Demonstration Plan (2011). http://www1.eere.energy.gov/hydrogenandfuelcells/mypp/pdfs/fuel_cells.pdf.
- [5] M.K. Debe, Advanced cathode catalysts and support for PEM fuel cells, in: Dept. of Energy Hydrogen Program Review, Washington DC, 2010. http://www.hydrogen.energy.gov/pdfs/review10/fc001_debe_2010_o_web.pdf.
- [6] K. Wipke, S. Sprick, J. Kurtz, T. Ramsden, in: 2010 Department of Energy Annual Merit Review and Peer Evaluation Meeting, Washington DC, June 10, 2010. http://www.hydrogen.energy.gov/pdfs/review10/tv001_wipke_2010_o_web.pdf.
- [7] F.A. de Bruijn, V.A.T. Dam, G.J.M. Janssen, *Fuel Cells* 8 (2008) 3–22.
- [8] R. Borup, J. Meyers, B. Pivovar, Y.S. Kim, R. Mukundan, N. Garland, D. Myers, M. Wilson, F. Garzon, D. Wood, P. Zelenay, K. More, K. Stroh, T. Zawodzinski, J. Boncella, J.E. McGrath, M. Inaba, K. Miyatake, M. Hori, K. Ota, Z. Ogumi, S. Miyata, A. Nishikata, Z. Siroma, Y. Uchimoto, K. Yasuda, K.I. Kimijima, N. Iwashita, *Chem. Rev.* 107 (2007) 3904–3951.
- [9] J. St-Pierre, N.Y. Jia, *J. New Mater. Electrochem. Syst.* 5 (2002) 263–271.
- [10] D. Chu, R.Z. Jiang, *J. Power Sources* 83 (1999) 128–133.
- [11] D. Chu, R.Z. Jiang, *J. Power Sources* 80 (1999) 226–234.
- [12] J. St-Pierre, D.P. Wilkinson, S. Knights, M.L. Bos, *J. New Mater. Electrochem. Syst.* 3 (2000) 99–106.
- [13] J.F. Wu, X.Z. Yuan, J.J. Martin, H.J. Wang, D.J. Yang, J.L. Qiao, J.X. Ma, *J. Power Sources* 195 (2010) 1171–1176.

- [14] M. Miller, A. Bazylak, J. Power Sources 196 (2011) 601–613.
- [15] Pucheng Pei, Xing Yuan, Pengxiang Chao, Xizhong Wang, Int. J. Hydrogen Energy 35 (2010) 3147–3151.
- [16] A.B. Bose, R. Shaik, J. Mawdsley, J. Power Sources 182 (2008) 61–65.
- [17] United States Department of Energy, Durability Test Protocol for PEM Fuel Cells (2005).
- [18] H.A. Gasteiger, W. Gu, R. Makharia, M.F. Mathias, B. Sompalli, Handbook of Fuel Cells – Fundamentals, Technology and Applications, vol. 3, Wiley, Chichester, UK, 2003, pp. 593–610.
- [19] S.S. Kocha, Handbook of Fuel Cells – Fundamentals, Technology and Applications, vol. 3, Wiley, Chichester, UK, 2003, pp. 555–557.
- [20] P. Spinelli, C. Francia, E.P. Ambrosio, M. Lucariello, J. Power Sources 178 (2008) 517–524.
- [21] M.V. Williams, H.R. Kunz, J.M. Fenton, J. Electrochem. Soc. 152 (2005) A635–A644.
- [22] A. Parthasarathy, S. Srinivasan, A.J. Appleby, C.R. Martin, J. Electrochem. Soc. 139 (1992) 2530–2537.
- [23] K.C. Neyerlin, W.B. Gu, J. Jorne, H.A. Gasteiger, J. Electrochem. Soc. 153 (2006) A1955–A1963.
- [24] H.A. Gasteiger, S.S. Kocha, B. Sompalli, F.T. Wagner, Appl. Catal., B: Environ. 56 (2005) 9–35.
- [25] S.G. Goebel, U.S. Patent 6,960,404, 2005.
- [26] J.P. Maes, S. Lievens, Texaco, Inc., U.S. Patent 7,201,982, 2007.
- [27] F. Barbir, PEM Fuel Cells, Elsevier Academic Press, Massachusetts, 2005.
- [28] P.J. Ferreira, G.J. la O', Y. Shao-Horn, D. Morgan, R. Makharia, S. Kocha, H.A. Gasteiger, J. Electrochem. Soc. 125 (2005) A2256–A2271.
- [29] S. Kundu, M.W. Fowler, L.C. Simon, R. Abouatallah, N. Beydokhti, J. Power Sources 183 (2008) 619–628.
- [30] S.G. Kandlikar, Z.J. Lu, Appl. Therm. Eng. 29 (2009) 1276–1280.
- [31] Y. Shao-Horn, W.C. Sheng, S. Chen, P.J. Ferreira, E.F. Holby, D. Morgan, Top. Catal. 46 (2007) 285–305.
- [32] R. Borup, J.R. Davey, F.H. Garzon, D.L. Wood, M.A. Inbody, J. Power Sources 163 (2006) 76–81.
- [33] M. Schulze, A. Schneider, E. Gulzow, J. Power Sources 127 (2004) 213–221.